Implementation of a frequency-dependent impedance boundary model into a room acoustic solver with time-domain finite element method

Yoshida, Takumi
Okuzono, Takeshi
Sakagami, Kimihiro

(Citation)
Acoustical Science and Technology,41(6):819-822

(Issue Date)
2020-11-01

(Resource Type)
journal article

(Version)
Version of Record

(URL)
https://hdl.handle.net/20.500.14094/90009297

ACOUSTICAL LETTER

Implementation of a frequency-dependent impedance boundary model into a room acoustic solver with time-domain finite element method

Takumi Yoshida[1,2,*], Takeshi Okuzono[2] and Kimihiro Sakagami[2]

[1]*Technical Research Institute, Hazama Ando Corporation, 515–1 Karima, Tsukuba, 305–0822 Japan*
[2]*Environmental Acoustic Laboratory, Department of Architecture, Graduate School of Engineering, Kobe University, 1–1 Rokkodai-cho, Nada-ku, Kobe, 657–8501 Japan*

(*Received 28 May 2020, Accepted for publication 16 June 2020*)

Keywords: FEM, Room acoustics simulation, Time domain frequency-dependent impedance boundary
PACS number: 43.55.Br, 43.55.Ka, 43.55.Dt [doi:10.1250/ast.41.819]

1. Introduction

A room acoustic solver with time-domain finite element method (TD-FEM) is a recently developed time-domain wave-based solver with inherent benefits for modeling complex geometries [1–6]. In general, performing reliable room acoustic simulations using extended-reacting sound absorber models that can incorporate frequency and incident angle dependence of sound absorption characteristics is important. However, acoustic TD-FEM has conventionally used a frequency-independent locally reacting impedance boundary model to treat sound absorbers because of its simple implementation. Some earlier works [3–5] investigating acoustic TD-FEM have used an extended-reacting model for a specific sound absorber, but difficulties in time-domain sound absorber modeling for TD-FEM have not been resolved yet. The present paper addresses frequency-dependent locally reacting impedance boundaries as a basis of constructing an efficient extended-reacting model.

A salient difficulty in time-domain absorber modeling derives from the necessity of considering frequency-dependence of various absorbers efficiently because its direct incorporation demands convolution computation. It diminishes the applicable range of TD-FEM as room acoustic solver because of the significant increase of computational costs. In recent years, an auxiliary differential equations (ADE) method [7] has been proposed to perform convolution computation indirectly with low computational costs. The ADE method can reflect frequency-dependent behaviors on time-domain simulations by solving additional first-order differential equations instead of the convolution computation. Then, the accuracy of time integration method for solving the additional differential equations affects that of the total system. The ADE method has been applied to other time-domain methods treating first-order differential equation (the continuity equation and Euler equation) [8,9] for dealing with frequency-dependence of boundaries. However, no report to date has described a study of the applicability of ADE method against acoustic TD-FEM treating second-order differential equation (wave equation).

Using the ADE method, this study examines a proposed room acoustic solver using TD-FEM to address frequency-dependent locally reacting impedance boundaries. We demonstrate the validity of formulation via numerical impedance problems to calculate normal incidence sound absorption characteristics, and include an examination of the time integration methods used for ADE method.

*e-mail: yoshida.takumi@ad-hzm.co.jp

2. Theory

2.1. Semi-discretized matrix equation of acoustic TD-FEM with impedance boundary

This study includes consideration of an interior sound field Ω described by the nonhomogeneous wave equation expressed in sound pressure p as

$$\frac{\partial^2 p}{\partial t^2} - c_0^2 \nabla^2 p = \rho_0 c_0^2 \frac{\partial q}{\partial t}, \tag{1}$$

where ρ_0 stands for the air density, c_0 denotes the speed of sound in air, and q represents the added fluid mass per unit volume. Application of finite element discretization and incorporation of three boundary conditions (a rigid boundary, a vibrating boundary and a locally reacting impedance boundary) engender the following semi-discretized matrix equation as

$$\boldsymbol{M}\ddot{\boldsymbol{p}} + c_0^2 \boldsymbol{K}\boldsymbol{p} + c_0 \boldsymbol{C}[y * \dot{\boldsymbol{p}}] = \boldsymbol{f}, \tag{2}$$

where

$$\boldsymbol{M} = \sum^{N_e} \int \boldsymbol{N}^T \boldsymbol{N} d\Omega_e,$$
$$\boldsymbol{K} = \sum^{N_e} \int \nabla \boldsymbol{N}^T \nabla \boldsymbol{N} d\Omega_e,$$
$$\boldsymbol{C} = \sum^{N_b} \int \boldsymbol{N}^T \boldsymbol{N} d\Gamma_e. \tag{3}$$

Here, $\boldsymbol{M}$, $\boldsymbol{K}$, and $\boldsymbol{C}$ respectively denote the mass matrix, the stiffness matrix and the dissipation matrix. Furthermore, $\boldsymbol{p}$, $\boldsymbol{f}$ and c_0 respectively denote the sound pressure vector, the external force vector, and the sound speed in air. Also, y denotes the specific admittance ratio on boundary surfaces, which is the reciprocal of the specific acoustic impedance ratio z. This study uses y instead of z in the approximation of rational function form as described later in this paper. The symbols $\cdot$, $\cdot\cdot$, and $*$ respectively denote first-order and second-order time derivatives and the convolution integral. Also, $\boldsymbol{N}$

represents a shape function. N_e and N_b respectively signify the numbers of acoustic elements and surface elements. $d\Omega_e$ and $d\Gamma_e$ respectively represent the volume integral and surface integral in an element. To deal with frequency-dependent impedance boundaries, the time-domain matrix equation of Eq. (2) involves convolutions as

$$y * \dot{\boldsymbol{p}} = \int_{-\infty}^{t} y(t-\tau)\dot{\boldsymbol{p}}(\tau)d\tau. \tag{4}$$

It is disadvantageous to perform the direct computation of the convolution in terms of computational efficiency because a coefficient matrix in the resulting linear system must be reconstructed at each time step. Moreover, the computation with many time steps leads to marked increases of required memory and computational times.

2.2. Auxiliary differential equations method

We use the ADE method to implement frequency-dependent impedance boundaries efficiently into the above TD-FEM. In the ADE method, the frequency-dependent surface admittance $y(\omega)$ is first approximated as the following rational function form of

$$y(\omega) \approx y_\infty + \sum_{i=1}^{n_{rp}} \frac{A_i}{\lambda_i + j\omega} + \sum_{i=1}^{n_{cp}} \left(\frac{B_i - jC_i}{\alpha_i - j\beta_i + j\omega} + \frac{B_i + jC_i}{\alpha_i + j\beta_i + j\omega} \right). \tag{5}$$

Here, ω and j respectively stand for the angular frequency and the imaginary unit $j^2 = -1$. Also, n_{rp} and n_{cp} respectively represent numbers of real poles and pairs of complex conjugate poles. y_∞, λ_i, α_i, β_i, A_i, B_i, and C_i are all real parameters that are accessible using various data fitting techniques. This study uses the vector fitting method [10]. Additionally, λ_i and α_i must be positive values to ensure convergence in time-domain computation. Using the approximated rational expression of surface admittance, the convolution computation in Eq. (4) is performed as

$$y * \dot{\boldsymbol{p}} \approx y_\infty \dot{\boldsymbol{p}} + \left(\sum_{i=1}^{n_{rp}} A_i \boldsymbol{\phi}_i + 2 \sum_{i=1}^{n_{cp}} (B_i \boldsymbol{\psi}_i^{(1)} + C_i \boldsymbol{\psi}_i^{(2)}) \right), \tag{6}$$

where the auxiliary functions $\boldsymbol{\phi}_i$, $\boldsymbol{\psi}_i^{(1)}$ and $\boldsymbol{\psi}_i^{(2)}$ are designated as the accumulators, which are denoted respectively as

$$\boldsymbol{\phi}_i = \int_{-\infty}^{t} e^{-\lambda_i(t-\tau)} \dot{\boldsymbol{p}}(\tau)d\tau, \tag{7}$$

$$\boldsymbol{\psi}_i^{(1)} = \int_{-\infty}^{t} e^{-\alpha_i(t-\tau)} \cos(\beta_i(t-\tau)) \dot{\boldsymbol{p}}(\tau)d\tau, \tag{8}$$

$$\boldsymbol{\psi}_i^{(2)} = \int_{-\infty}^{t} e^{-\alpha_i(t-\tau)} \sin(\beta_i(t-\tau)) \dot{\boldsymbol{p}}(\tau)d\tau. \tag{9}$$

The following first-order time differentiations of Eqs. (7)–(9) are used to compute time-marching of the accumulators.

$$\dot{\boldsymbol{\phi}}_i + \lambda_i \boldsymbol{\phi}_i = \dot{\boldsymbol{p}}, \tag{10}$$

$$\dot{\boldsymbol{\psi}}_i^{(1)} + \alpha_i \boldsymbol{\psi}_i^{(1)} + \beta_i \boldsymbol{\psi}_i^{(2)} = \dot{\boldsymbol{p}}, \tag{11}$$

$$\dot{\boldsymbol{\psi}}_i^{(2)} + \alpha_i \boldsymbol{\psi}_i^{(2)} - \beta_i \boldsymbol{\psi}_i^{(1)} = \boldsymbol{0}. \tag{12}$$

The total system stability and accuracy depend on the time integration method applied to calculate the time-marching of accumulators. The ADE method can reflect frequency-dependence accurately without use of small time interval by using higher-order numerical methods. It will be shown in the subsequent numerical results with explicit Runge-Kutta methods (RKM) having different order of accuracy.

2.3. Construction of a new time-marching scheme

With the ADE method, the semi-discretized equation Eq. (2) can be rewritten as

$$\boldsymbol{M}\ddot{\boldsymbol{p}} + c_0^2 \boldsymbol{K}\boldsymbol{p} + c_0 \boldsymbol{C} y_\infty \dot{\boldsymbol{p}} = \boldsymbol{f} - c_0 \boldsymbol{C} \left(\sum_{i=1}^{n_{rp}} A_i \boldsymbol{\phi}_i + 2 \sum_{i=1}^{n_{cp}} (B_i \boldsymbol{\psi}_i^{(1)} + C_i \boldsymbol{\psi}_i^{(2)}) \right). \tag{13}$$

In the temporal direction, application of the Newmark β method engenders the following time-marching scheme to calculate interior sound fields including locally reacting frequency-dependent admittance boundaries.

$$\left(\boldsymbol{M} + \beta^* c_0^2 \Delta t^2 \boldsymbol{K} + \frac{c_0 \Delta t}{2} y_\infty \boldsymbol{C} \right) \ddot{\boldsymbol{p}}^{n+1} = \boldsymbol{f}^{n+1} - c_0^2 \boldsymbol{K}\boldsymbol{P}_1 - c_0 \boldsymbol{C}(y_\infty \boldsymbol{P}_2 + \boldsymbol{P}_3), \tag{14}$$

$$\boldsymbol{p}^{n+1} = \boldsymbol{p}^n + \Delta t \dot{\boldsymbol{p}}^n + \Delta t^2 \left(\left(\frac{1}{2} - \beta^* \right) \ddot{\boldsymbol{p}}^n + \beta^* \ddot{\boldsymbol{p}}^{n+1} \right), \tag{15}$$

$$\dot{\boldsymbol{p}}^{n+1} = \dot{\boldsymbol{p}}^n + \frac{\Delta t}{2} (\ddot{\boldsymbol{p}}^n + \ddot{\boldsymbol{p}}^{n+1}), \tag{16}$$

with

$$\boldsymbol{P}_1 = \boldsymbol{p}^n + \Delta t \dot{\boldsymbol{p}}^n + \Delta t^2 \left(\frac{1}{2} - \beta^* \right) \ddot{\boldsymbol{p}}^n, \tag{17}$$

$$\boldsymbol{P}_2 = \dot{\boldsymbol{p}}^n + \frac{\Delta t}{2} \ddot{\boldsymbol{p}}^n, \tag{18}$$

$$\boldsymbol{P}_3 = \sum_{i=1}^{n_{rp}} A_i \boldsymbol{\phi}_i^{n+1} + 2 \sum_{i=1}^{n_{cp}} (B_i \boldsymbol{\psi}_i^{(1)n+1} + C_i \boldsymbol{\psi}_i^{(2)n+1}). \tag{19}$$

Here, Δt, n and β^* respectively stand for the time interval, the time step and the parameter in the Newmark β method. Hereinafter, the conjugate gradient iterative solver with convergence tolerance of 10^{-4} was used for solving simultaneous linear equations of Eq. (14).

3. Numerical experiments

To demonstrate the formulation validity, we conducted numerical simulations of normal incidence sound absorption coefficient measurement based on transfer function method with the three-dimensional impedance tube model shown in

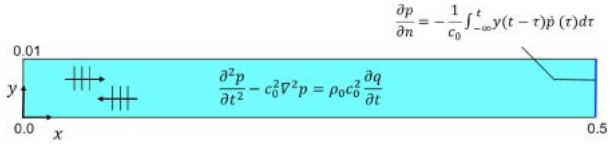

Fig. 1 An x–y cross section of the analyzed impedance tube model with a frequency-dependent impedance boundary.

Fig. 1. The impedance tube is 0.5 m long, with a 0.01×0.01 m^2 cross-sectional area. In addition, a boundary surface at $x = 0.5$ m has a frequency-dependent impedance boundary of rigid-backed porous sound absorbers calculated using a theory based on an equivalent fluid model [11], i.e., $Z = -jZ_c \cot(k_e d)$, where Z, Z_c and k_e respectively represent the specific acoustic impedance of absorber surface, the characteristic impedance and the complex wavenumber of equivalent fluid. In addition, d represents the material thickness; Z_c and k_e were calculated using Miki's empirical equation [12]. At the tube inlet, we assumed a plane wave incidence with the waveform of Gaussian pulse having upper-limit frequency of 10 kHz. The model was discretized spatially with a dispersion-reduced 8-node cubic element [1] of 0.005 m. The number of points per wavelength of the FE mesh was 6.87 at 10 kHz. We set $c_0 = 343.7$ m/s. In the temporal direction, fourth-order accurate Fox–Goodwin method, which is a Newmark β method with the parameter $\beta^* = 1/12$, is employed. The stability condition of present TD-FEM in air region is given as $\Delta t_{\text{limit}} \leq \frac{h}{c_0\sqrt{3}}$ [1], where Δt_{limit} and h respectively stand for the stability limit of time interval value and an element size.

3.1. Effects of time integration methods on accuracy

As a first step, we examined the effect of time accuracy of explicit RKM applied for time-marching of accumulators on the modeling of frequency-dependent impedance boundary. We tested RKMs of four kinds with different orders of accuracy, which are, respectively, first-order accurate method [13] (RKM1), second-order accurate method [14] (RKM2), fourth-order accurate method [13] (RKM4), and sixth-order accurate method [15] (RKM6). For each method, Δt was set to a numerically determined critical time interval $m\Delta t_{\text{limit}}$, for which a constant m was determined numerically. In the simulation, a porous absorber with flow resistivity $R = 13{,}000$ Pa s/m^2, and thickness $d = 0.025$ m was considered. The acoustic admittance of the porous absorber was approximated by rational function with $n_{\text{rp}} = 3$ and $n_{\text{cp}} = 2$. Figure 2 compares normal incidence absorption coefficient α_0 and surface impedance z calculated using the theory and the fitted rational function model, showing excellent agreement in broadband.

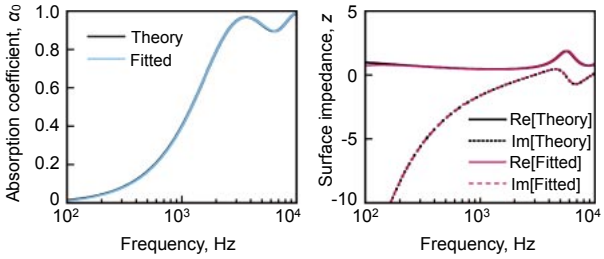

Fig. 2 Comparisons of absorption coefficient α_0 (left) and surface impedance z (right) calculated using theory and the fitted rational function model.

Figure 3 presents comparisons of α_0 and z calculated using the fitted model and the present TD-FEM with RKMs of four kinds. Only the low-order RKM1 showed worse stability with $m = 0.85$. Other higher-order methods showed good stability with $m = 1$. The results showed that RKM1 exhibits large discrepancy from the fitted model results in both α_0 and z. The other three higher-order RKMs agree better with the fitted model; also, RKM4 and RKM6 shows excellent agreement. These results suggest that higher-order RKM4 is efficient for accurate analysis with larger time interval. Also, it needs the storage of only single time step history, and no matrix operations are included.

3.2. Further examination using different porous absorbers

Subsequently, we tested the robustness of present TD-FEM further using RKM4 in three other cases with porous absorbers having different flow resistivity and thickness. The following three cases were tested: (a) $R = 13{,}000$ Pa s/m^2 and $d = 0.05$ m, (b) $R = 50{,}000$ Pa s/m^2 and $d = 0.025$ m, and (c) $R = 50{,}000$ Pa s/m^2 and $d = 0.05$ m. The surface admittances of the absorbers were approximated respectively by the rational function with (a) $n_{\text{rp}} = 3$ and $n_{\text{cp}} = 4$, (b) $n_{\text{rp}} = 3$ and $n_{\text{cp}} = 3$, and (c) $n_{\text{rp}} = 3$ and $n_{\text{cp}} = 2$. Figure 4 presents

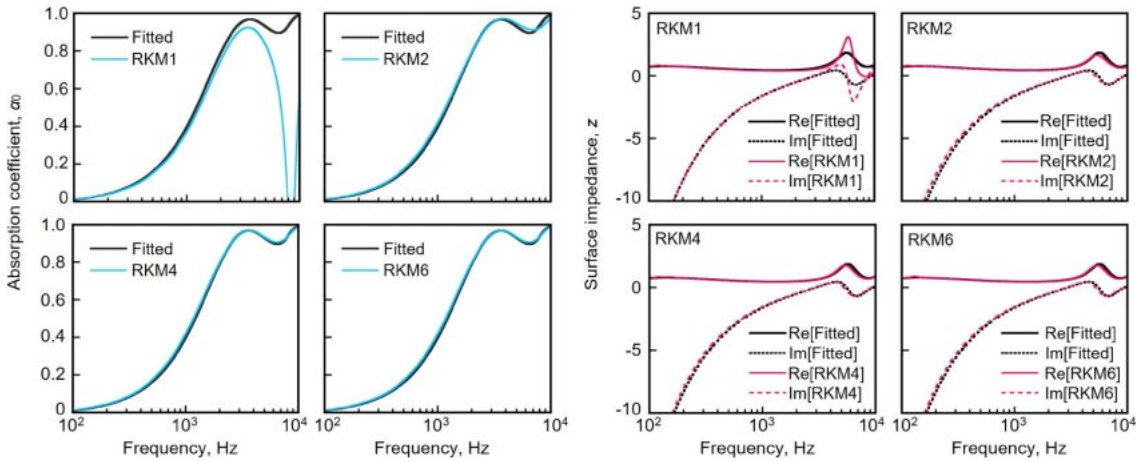

Fig. 3 Comparisons of absorption coefficient α_0 (left) and surface impedance z (right) of porous absorber with $R = 13{,}000$ Pa s/m^2 and $d = 0.025$ m calculated using the fitted rational function model and RKM1, RKM2, RKM4, and RKM6.

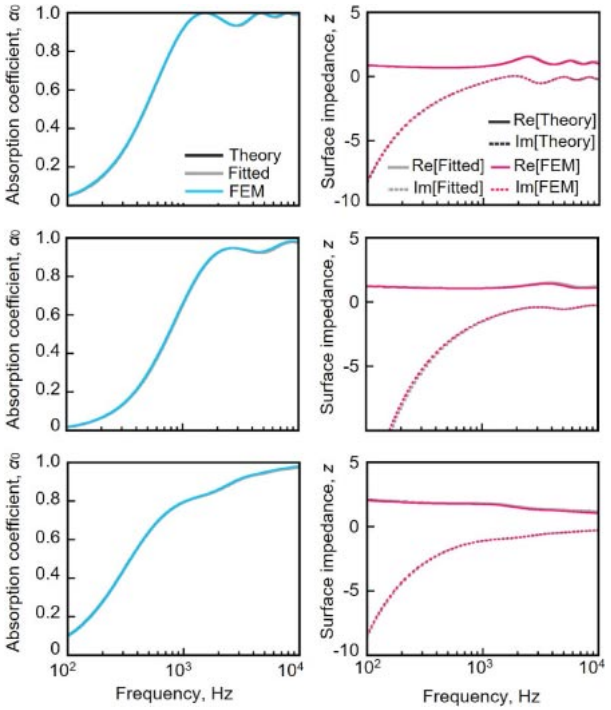

Fig. 4 Comparisons of absorption coefficient α_0 (left) and surface impedance z (right) of porous absorbers with $R = 13{,}000\,\mathrm{Pa\,s/m^2}$ and $d = 0.025\,\mathrm{m}$ (upper), $R = 50{,}000\,\mathrm{Pa\,s/m^2}$ and $d = 0.025\,\mathrm{m}$ (middle), and $R = 50{,}000\,\mathrm{Pa\,s/m^2}$ and $d = 0.05\,\mathrm{m}$ (lower) calculated using theory, a fitted rational function model, and TD-FEM.

comparisons of α_0 and z of three kinds porous absorbers calculated using the theory, the fitted rational function model and the present TD-FEM. Results showed that the present TD-FEM can simulate broadband frequency-dependent absorption characteristics accurately in various conditions. Moreover, stable computations with $m = 1$ were possible in all cases.

4. Conclusion

This paper proposed an efficient TD-FEM able to incorporate broadband frequency-dependent impedance boundaries using ADE method. The numerical impedance tube problems to calculate normal incidence sound absorption characteristics showed the validity of proposed formulation. In addition, results show that a fourth-order accurate explicit RKM is accurate and stable in time-marching calculations of accumulators. The ADE method is applicable to explicit TD-FEM and to time-domain porous models to assess extended-reacting conditions. Relevant results will be presented in the near future.

References

[1] T. Okuzono, T. Otsuru, R. Tomiku and N. Okamoto, "Application of modified integration rule to time-domain finite-element acoustic simulation of rooms," *J. Acoust. Soc. Am.*, **132**, 804–813 (2012).

[2] T. Yoshida, T. Okuzono and K. Sakagami, "Numerically stable explicit time-domain finite element method for room acoustics simulation using an equivalent impedance model," *Noise Control Eng. J.*, **66**, 176–189 (2018).

[3] T. Yoshida, T. Okuzono and K. Sakagami, "A three-dimensional time-domain finite element method based on first-order ordinary differential equations for treating permeable membrane absorbers," *Proc. 25th Int. Congr. on Sound Vib.*, 838, 7 pages (2018).

[4] T. Okuzono, N. Shimizu and K. Sakagami, "Predicting absorption characteristics of single-leaf permeable membrane absorbers using finite element method in a time domain," *Appl. Acoust.*, **151**, 172–182 (2019).

[5] T. Yoshida, T. Okuzono and K. Sakagami, "A locally implicit time domain FEM for room acoustics simulation including permeable membrane absorbers," *Proc. 23rd Int. Congr. Acoust.*, pp. 763–770 (2019).

[6] T. Okuzono, K. Sakagami and T. Osturu, "Dispersion-reduced time domain FEM for room acoustics simulation," *Proc. 23rd Int. Congr. Acoust.*, pp. 6070–6077 (2019).

[7] D. Dragna, P. Pineau and P. Blanc-Benon, "A generalized recursive convolution method for time-domain propagation in porous media," *J. Acoust. Soc. Am.*, **138**, 1030–1042 (2015).

[8] F. Pind, A. P. Engsig-Karup, C. H. Jeong, J. S. Hesthaven, M. S. Mejling and J. Strømann-Anderson, "Time domain room acoustic simulations using the spectral element method," *J. Acoust. Soc. Am.*, **145**, 3299–3310 (2019).

[9] H. Wang and M. Hornikx, "Time-domain impedance boundary condition modeling with the discontinuous Galerkin method for room acoustics simulations," *J. Acoust. Soc. Am.*, **147**, 2534–2546 (2020).

[10] B. Gustavsen and A. Semlyen, "Rational approximation of frequency domain responses by vector fitting," *IEEE Trans. Pow. Del.*, **14**, 1052–1061 (1999).

[11] J. F. Allard and N. Atalla, "Acoustic impedance at normal incidence of fluids. Substitution of a fluid layer for a porous layer," in *Propagation of Sound in Porous Media: Modeling Sound Absorbing Materials*, 2nd ed. (John Wiley & Sons, Chichester, 2009), Chap. 2, pp. 15–27.

[12] Y. Miki, "Acoustical properties of porous materials — Modification of Delany-Bazley models —," *J. Acoust. Soc. Jpn.* (*E*), **11**, 19–24 (1990).

[13] P. O. J. Scherer, "Equations of motion," in *Computational Physics: Simulation of Classical and Quantum Systems*, 3rd ed. (Springer Nature, Berlin/Heidelberg, 2017), Chap. 13, pp. 292–303.

[14] A. Ralston, "Runge–Kutta methods with minimum error bounds," *Math. Comput.*, **16**, 431–437 (1962).

[15] J. C. Butcher, "On Runge–Kutta processes of high order," *J. Aust. Math. Soc.*, **4**, 179–194 (1964).